Hindawi
International Journal of Photoenergy
Volume 2017, Article ID 7190801, 9 pages
https://doi.org/10.1155/2017/7190801

Research Article

Effect of Annealing Process on $CH_3NH_3PbI_{3-X}Cl_X$ Film Morphology of Planar Heterojunction Perovskite Solar Cells with Optimal Compact TiO_2 Layer

Dan Chen, Xiaoping Zou, Hong Yang, Ningning Zhang, Wenbin Jin, Xiao Bai, and Ying Yang

Research Center for Sensor Technology, Beijing Key Laboratory for Sensor, Ministry of Education Key Laboratory for Modern Measurement and Control Technology, School of Applied Sciences, Beijing Information Science and Technology University, Jianxiangqiao Campus, Beijing 100101, China

Correspondence should be addressed to Xiaoping Zou; xpzou2014@163.com

Received 23 May 2017; Revised 4 August 2017; Accepted 13 August 2017; Published 8 November 2017

Academic Editor: Matthias Auf der Maur

The morphology of compact TiO_2 film used as an electron-selective layer and perovskite film used as a light absorption layer in planar perovskite solar cells has a significant influence on the photovoltaic performance of the devices. In this paper, the spin coating speed of the compact TiO_2 is investigated in order to get a high-quality film and the compact TiO_2 film exhibits pinhole- and crack-free films treated by 2000 rpm for 60 s. Furthermore, the effect of annealing process, including annealing temperature and annealing program, on $CH_3NH_3PbI_{3-X}Cl_X$ film morphology is studied. At the optimal annealing temperature of 100°C, the $CH_3NH_3PbI_{3-X}Cl_X$ morphology fabricated by multistep slow annealing method has smaller grain boundaries and holes than that prepared by one-step direct annealing method, which results in the reduction of grain boundary recombination and the increase of Voc. With all optimal procedures, a planar fluorine-doped tin oxide (FTO) substrate/compact TiO_2/$CH_3NH_3PbI_{3-X}Cl_X$/Spiro-MeOTAD/Au cell is prepared for an active area of 0.1 cm^2. It has achieved a power conversion efficiency (PCE) of 14.64%, which is 80.3% higher than the reference cell (8.12% PCE) without optimal perovskite layer. We anticipate that the annealing process with optimal compact TiO_2 layer would possibly become a promising method for future industrialization of planar perovskite solar cells.

1. Introduction

Perovskite solar cells (PSCs) have developed a variety of device structures, since the first report from Kojima et al. in 2009 [1], such as mesoporous, meso-superstructure, planar heterojunction, and hole-blocking layer-free structure [2–5]. The planar heterojunction is considered to be the most competitive construction on account of their simplified fabricating procedure. Up to date, several materials could be chosen as electron-selective layer (ESL), for instance, ZnO [6, 7], TiO_2 [8], Zn_2SnO_4 [9], SnO_2 [10], fullerene, PCBM [11] and so on. And many different advanced thin-film technologies have been developed for obtaining high-quality perovskite layer, such as one-step spin coating [2], two-step deposition [8, 12, 13], vapor-assisted solution process [14], dual-source thermal evaporation [4], compositional engineering [15], and interface engineering [16]. Compact TiO_2 (c-TiO_2) film and $CH_3NH_3PbI_{3-X}Cl_X$ film are the most commonly used materials in planar heterojunction PSCs due to the excellent ability of carrier extraction and long carrier diffusion length [17], respectively. However, no matter what material is chosen or how method is adopted, the morphology of both two layers is regarded as one of the most critical issues.

The ESL acts as the blocking layer to prevent photogenerated holes from reaching the FTO substrate, which would or else short circuit the device. Karthikeyan and Thelakkat demonstrated that an optimum thickness of c-TiO_2 film, which prepared by spray pyrolysis deposition, was 120–150 nm for the high cell performance in 2008 [18]. Excellent layer thickness obtained for c-TiO_2 film employed by spin coating method was 80–180 nm, which was reported by Kim [2]. Lellig reported that the best values of c-TiO_2 film ranged

from 40 to 70 nm by using an amphiphilic diblock copolymer as a functional template [19]. It must be mentioned that spin coating is the most frequently used method owing to exceptional advantages such as easy operation and low cost. Several excellent reviews so far have focused on the optimum thickness of the ESL, nonetheless, no systematic study concerning the effect of spin coating rate on the morphology of ESL.

It is commonly known that $CH_3NH_3PbI_{3-X}Cl_X$ film has appealing physical properties, for example, broad light absorption range, high extinction coefficients, a small exciton binding energy, and a tunable bandgap. Accompanied by recent developments of improving the quality of the light absorption layer, the PCE of PSCs has risen from 3.8% [1] to 22.1% [20]. For typical annealing program, Huang et al. showed the highest efficiency of ~13.58% in PSCs with Ag electrode and 0.07 cm^2 active area by multistep slow annealing method for the ultimate temperature of 95°C in 2015 [21]. It is worthwhile mentioning that the annealing procedure, including annealing temperature and annealing program, has an essential influence on $CH_3NH_3PbI_{3-X}Cl_X$ film morphology, in spite of many efforts that have been reported to control the quality of the light harvest layer.

In this article, we show that the most excellent rate for the spin coating ESL is 2000 rpm for 60 s. Moreover, two different programs, one-step (OS) direct annealing method and multistep (MS) slow annealing method, are employed to prepare the high-quality perovskite film. We reveal that the best temperature of OS direct annealing method is 100°C. The average PCE of MS devices is 47.3% higher than that of devices produced by OS method results from the smaller grain boundary recombination and the higher Voc and FF. Our solar cell with the Au electrode, 0.1 cm^2 active area, and optimal compact TiO_2 layer has achieved a best power conversion efficiency (PCE) of 14.64% by MS annealing method for the ultimate temperature of 100°C.

2. Experimental and Methods

2.1. Materials. The zinc powder was purchased from Sinopharm Chemical Reagent Beijing Co. Ltd. and Au from ZhongNuo Advanced Material Technology Co. Ltd. Isopropanol was purchased from Beijing Chemical Works (AR) or Sigma-Aldrich (99.8%). Ethanol, acetone, diethyl ether, and hydrochloric acid were purchased from Beijing Chemical Works, and $TiCl_4$, methylamine alcohol (33%), and hydrogen iodide (HI, 55%–58%) were purchased from Aladdin Industrial Corporation. $PbCl_2$, N,N-dimethylformamide (99.8%), isopropyl titanate (99.8%), 4-tert-butylpyridine (TBP, 96%), Spiro-MeOTAD (2,2′,7,7′-tetrakis-(N,N-di-p-methoxyphenylamine)-9,9′-spirobifluorene), chlorobenzene, acetonitrile, and Li-bis (trifluoromethanesulfonyl) imide (Li-TFSI) ($C_2F_6LiNO_4S_2$, 99.95%) were purchased from Sigma-Aldrich. Deionized water was prepared by Research Center for Sensor Technology, Beijing Key Laboratory for Sensor, Beijing Information Science and Technology University.

2.2. The Preparation of Precursor. Hydrochloric (HCl) acid solution (4 mol/L) was prepared by mixing deionized water (667 mL) into hydrochloric acid (333 mL, 12 mol/L). 2 M HCl (35 mL) was dissolved in 2.53 ml of isopropanol (AR), and the mixture was defined as A solution. Isopropyl titanate solution was fabricated by dissolving 369 μg isopropyl titanate in 2.53 ml of isopropanol (99.8%), to which the A solution was added drop by drop by high rate stirring, and then the final solution was filtered. CH_3NH_3I was synthesized by stirring the mixture solution of methylamine alcohol (24 mL, 33 wt%) and hydrogen iodide (HI, 55–58 wt%) at 0°C for 2 h. The mixture was evaporated in a rotavap, and the remaining solid was washed with diethyl ether and dried three times. The formation of white powder indicated the successful crystallization. $CH_3NH_3PbI_{3-x}Cl_x$ perovskite precursor solution was prepared as follows. 0.244 g $PbCl_2$ (0.88 mM) and 0.42 g CH_3NH_3I (2.64 mM) were dissolved in 1 mL N,N-dimethylformamide. The mixture was stirred for 180 min at 90°C. 520 mg of Li-TFSI was dissolved in 1 mL acetonitrile, and the mixture was defined as B solution. 72.3 mg of Spiro-MeOTAD and 28.8 μL of TBP were dissolved in chlorobenzene (1 mL), to which the B solution (17.5 μL) was added and stirred, in order to prepare the hole transport material precursor solution.

2.3. Device Fabrication. The FTO (1.5 × 1.5 cm^2, <14 Ω/sq, 2.2 mm thick, Pilkington, Solar Energy Technology Co. Ltd., Wuhan Jinge, China) substrates were firstly etched using Zn powder and hydrochloric acid solution for 2 min to form the retained area of 1.5 × 1.0 cm^2 as patterned electrode. The etched FTO substrates were cleaned according to the literature procedures [22]. And the following procedures were done in a nitrogen-filled glovebox. The isopropyl titanate solution was spin coated on the pretreated FTO to prepare the c-TiO_2 layer at 1000 rpm, 2000 rpm, and 3000 rpm for 60 s, before drying at 125°C for 10 min and then annealing at 500°C for 30 min. The ESLs were then immersed in 0.04 M of $TiCl_4$ aqueous solution to improve interface contact with the light harvester [23–25]. The c-TiO_2 layer was immersed in $TiCl_4$ aqueous solution for 30 min at 70°C. After washed with deionized water, the film was dried with N_2 flow and sintered at 500°C for 30 min. The $CH_3NH_3PbI_{3-x}Cl_x$ film was deposited on the ESL by spin coating the $CH_3NH_3PbI_{3-x}Cl_x$ perovskite precursor solution at 2000 rpm for 45 s and then treated by different calcined programs as follow. The annealing temperatures were directly raise to 90°C, 100°C, 110°C, 120°C, or 130°C for OS direct annealing method. The annealing time for every temperature was 90 min, which was chosen according to the literature [26]. For the MS slow annealing method, the annealing temperature was raised from 30°C to 100°C, and the annealing times for 30°C, 40°C, and 50°C were both 5 min, for 60°C, 70°C, 80°C, and 90°C were both 10 min, and the ultimate time was 90 min for 100°C. Once the $CH_3NH_3PbI_{3-X}Cl_X$ films deposited well, the hole transport material precursor solution was spin coated at 2000 rpm for 45 s. Finally, a metal contact electrode (~60 nm), such as Al or Au, was deposited on the Spiro-MeOTAD using thermal evaporation at a pressure of 1×10^{-6} mbar.

2.4. Material and Device Characterizations. The morphology of all films was observed with a field emission scanning

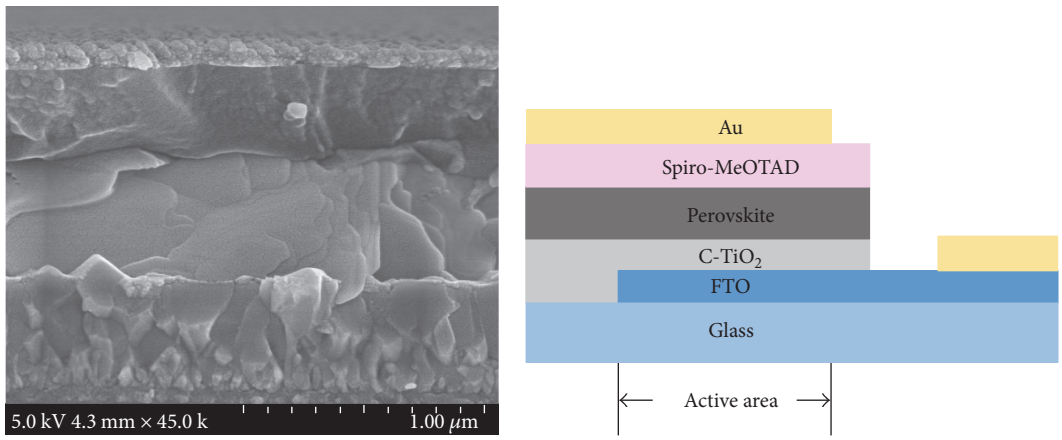

Figure 1: Representative cross-sectional SEM image (a) and schematic illustration (b) of the planar heterojunction perovskite solar cell.

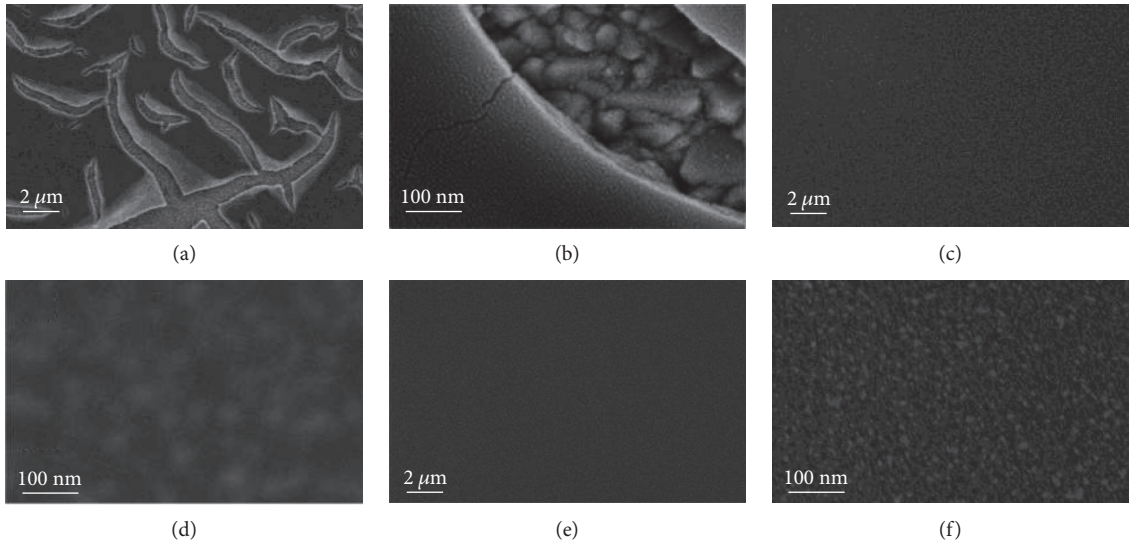

Figure 2: Top view SEM images of c-TiO_2 film with different spin coating speeds for 60 s. (a), (c), and (e) the low magnification and (b), (d), and (f) the high magnification images for 1000 rpm, 2000 rpm, and 3000 rpm, respectively.

electron microscope (FESEM, Hitachi S-4800). X-ray diffraction (XRD) patterns were performed with Bruker D8 Focus (Bruker Corporation, Germany) to analyze the crystal structure of the samples. UV-vis absorption spectra were measured by Cary 5000 (Varian, America). The current-voltage curves were characterized using a V3-400 (Princeton Applied Research) under AM 1.5G one sun illumination (100 mW/cm^2) with a scan rate of 0.1 V/s, which was simulated by solar simulator (Newport Oriel Class 3A) equipped with Xenon lamp (L2175). The thickness of TiO_2 ESL was characterized with NanoMap Surface Profiler (AEP Technology, USA).

3. Results and Discussion

3.1. Effect of the Different Spin Coating Speeds on the Morphology of the c-TiO_2 Film. Figure 1 presents a cross-sectional scanning electron microscopy (SEM) image of a representative planar heterojunction solar cell device. It is generally accepted that the perovskite material harvests light to generate hole-electron pairs and c-TiO_2 film suppresses the electrical contact between FTO and photovoltaic layer [27].

To achieve a better understanding of the effectiveness of the different spin coating speeds on the morphology of the c-TiO_2 film, the SEM images of three different speeds are showed in Figure 2. Figures 2(a), 2(c), and 2(e) are the low magnification, and Figures 2(b), 2(d), and 2(f) are the high magnification images of c-TiO_2 film for 1000 rpm, 2000 rpm, and 3000 rpm, respectively. The SEM images highlight the variation in the film surface morphology of the ELS. The speed of 2000 rpm produces better surface coverage and smaller film defect, as compared with the c-TiO_2 films prepared using other two speeds. The top views of a film prepared with 2000 rpm (Figures 2(c) and 2(d)) reveal that the FTO is fully covered by the more

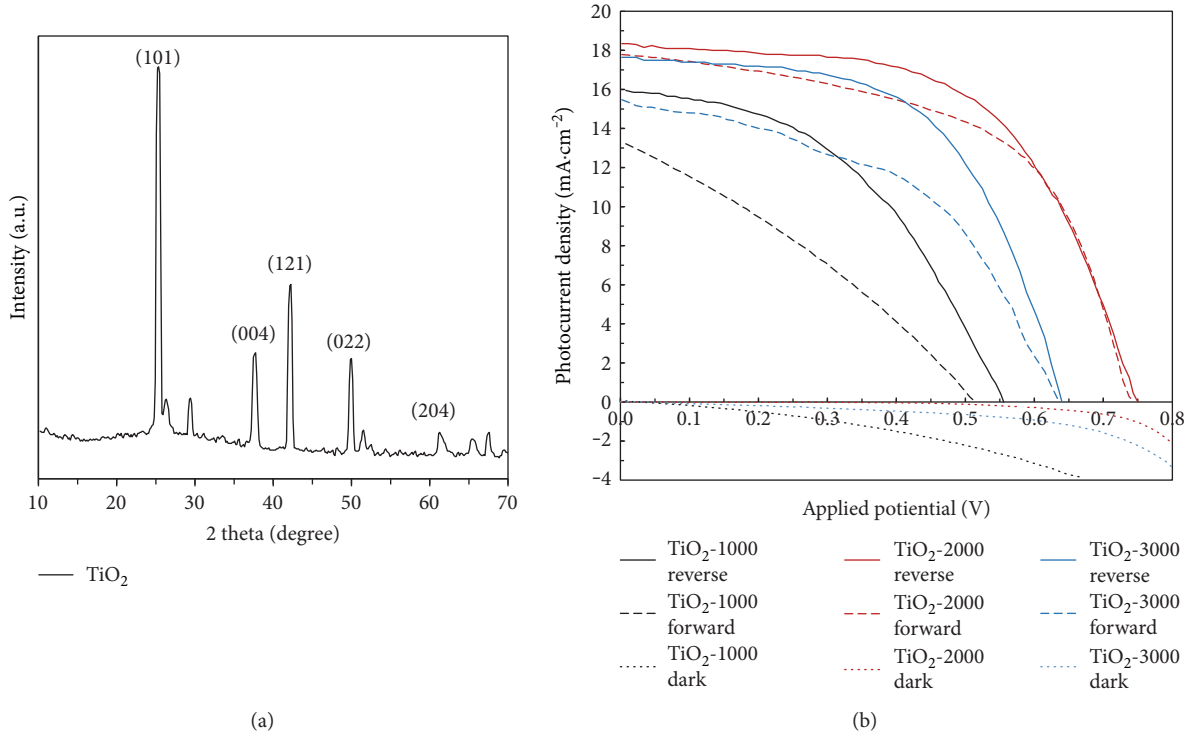

FIGURE 3: (a) XRD pattern of c-TiO_2 film prepared with 2000 rpm. (b) J-V characteristics of devices based on various c-TiO_2 films.

uniform and smooth c-TiO_2 layer. Especially, many cracks can be observed from the film when fabricated with the speed of 1000 rpm (Figures 2(a) and 2(b)), and numerous pinholes can be discovered from the film when obtained with speed of 3000 rpm (Figures 2(e) and 2(f)).

We analyze the phase purity of the c-TiO_2 film prepared with 2000 rpm by XRD (Figure 3(a)). For the c-TiO_2 film, the diffraction peaks are located at $2\theta = 25.3^\circ$ and 38.0°, corresponding to the 101 and 004 planes of the anatase structure of TiO_2 (JCPDS card number 21-1272). The diffraction peak of TiO_2 (101) plane showed a high intensity, indicating that the c-TiO_2 film by spin coating has a well-defined and high-purity anatase phase.

In this study, we prepare PSCs using three kinds of c-TiO_2 films as ELS by different spin coating speeds and measure the J-V curves of the devices with an active area of 0.1 cm^2 to investigate the influence of the rate on the ELS. Figure 3(b) shows the J-V curves of three best cells, and the detailed photovoltaics data extracted from the reversed J-V curves for these devices can be found in Table 1. Samples TiO_2-1000, TiO_2-2000, and TiO_2-3000 are corresponding to the devices manufactured with 1000 rpm, 2000 rpm, and 3000 rpm, respectively. From this data, the 2000 rpm cell gives a PEC of 8.12% corresponding to a J_{SC} of 18.3 mA·cm^{-2}, a Voc of 0.75 V, and a FF of 0.58 and has the lowest series resistance (R_s) which is ~7.59 Ω·cm^2. The good performance of this device is mainly due to a decrease in the R_s, as is apparent from Table 1. We attribute this lowest R_s to the best morphology of the c-TiO_2 films which has smaller cracks and pinholes, in contrast to the morphology of the 1000 rpm and 3000 rpm films. The

TABLE 1: Photovoltaic performance parameters extracted from reversed J-V curves (Figure 3(b)).

Sample	J_{sc}/mA·cm^{-2}	V_{oc}/V	FF/%	PCE/%	R_s/Ω·cm^2
TiO_2-1000	15.9	0.55	0.45	4.05	12.98
TiO_2-2000	18.3	0.75	0.58	8.12	7.59
TiO_2-3000	17.7	0.64	0.58	6.57	9.25

hysteresis observed in TiO_2-2000 cell is weak compared to the hysteresis in other two samples. The previous work investigates that the FTO/c-TiO_2 interface and c-TiO_2/$CH_3NH_3PbI_{3-X}Cl_X$ interface are the origins of hysteresis [28]. Furthermore, the deeper trap states, ferroelectric polarization, and ion migration may also be responsible for the hysteresis in PSCs. The dark J-V curves indicate that the device with 2000 rpm TiO_2 layer exhibits a better diode behaviour than the samples with other two kinds of TiO_2 layers. The direct contacts between $CH_3NH_3PbI_{3-X}Cl_X$ layer and FTO may be responsible for the poor rectification ability of the TiO_2-1000 and TiO_2-3000 cells [5].

According to Ke at al.'s work [29], the thickness of c-TiO_2 layer has a huge influence on the photovoltaic performance on the PSCs. We characterized the thickness of TiO_2 ESL using the surface profiler. The thicknesses of c-TiO2 layers prepared by 1000 rpm, 2000 rpm, and 3000 rpm are ~67 nm, ~47 nm, and ~36 nm, respectively. The 67 nm TiO_2 ESL is too thick to transfer the electron from the light absorption layer to the FTO. The too thin c-TiO_2 layer (36 nm) leads to a serious recombination process because the FTO is not fully covered with the c-TiO2 layers, and the light absorption

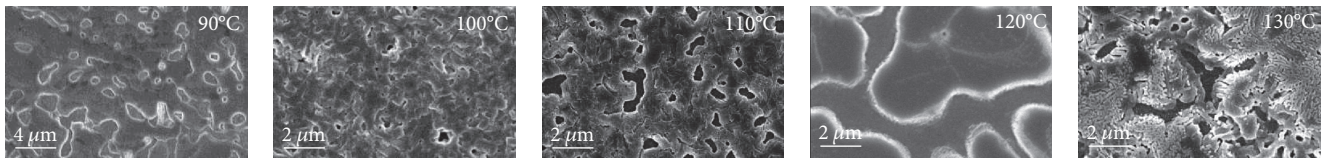

FIGURE 4: Top view SEM images of $CH_3NH_3PbI_{3-X}Cl_X$ films deposited on the c-TiO_2 layer with diverse OS annealing temperatures. (a) 90°C, (b) 100°C, (c) 110°C, (d) 120°C, and (e) 130°C.

layer contacts with the FTO directly. The optimum thickness of c-TiO2 layers is ~47 nm. In this article, we employ the c-TiO_2 film prepared by 2000 rpm method as the ELS in the following fabrication of PSCs due to its excellent photovoltaic performance.

3.2. Effect of the OS Direct Annealing Temperature on the Morphology of the Perovskite Film. Figure 4 exhibits the top view SEM images of $CH_3NH_3PbI_{3-X}Cl_X$ films deposited on the c-TiO_2 layer with diverse OS direct annealing temperatures of (a) 90°C, (b) 100°C, (c) 110°C, (d) 120°C, and (d) 130°C. As the annealing temperature increases from 90°C to 100°C, the number of pinholes is significantly decreased. At a temperature of 100°C, the perovskite films show denser packing and the coverage of perovskite film is obviously improved even though some c-TiO_2 still remains uncovered. However, as the annealing temperature increases from 110°C to 130°C, the c-TiO_2 layer uncovered with $CH_3NH_3PbI_{3-X}Cl_X$ films becomes pronounced due to the size of pinholes and is significantly increased and the perovskite film shows polydisperse perovskite islands. These consequences are in qualitative agreement with previous researches on the thermal annealing precursor of CH_3NH_3I and $PbCl_2$, where it was found that high temperatures resulted in the rapid growth from a few nucleation sites leading to the formation of large crystalline islands and the associated large gaps in between [30]. The increase in the uncovered c-TiO_2 with increasing annealing temperature indicates that the lower annealing temperature (100°C) is appropriate for the preparation of maximum coverage $CH_3NH_3PbI_{3-X}Cl_X$ films, which is consistent with the research in the literature [31].

In Figure 5, we compare the XRD patterns of $CH_3NH_3PbI_{3-X}Cl_X$ films prepared by different annealing temperatures and observe the appearance of a series of diffraction peaks that are in good agreement with the literature data on the orthorhombic phase of $CH_3NH_3PbI_{3-X}Cl_X$. The main diffraction peaks, assigned to the (110), (220), and (330) peaks at 13.99°, 28.36°, and 43.10°, respectively, are in identical positions for every temperature films, indicating that all temperatures have manufactured the same mixed-halide perovskite with an orthorhombic crystal structure [4, 32]. At a temperature of 90°C, the diffraction peaks are located at $2\theta = 15.5°$ and 31.3°, corresponding to the 100 and 200 planes of the single-phase of cubic $CH_3NH_3PbCl_3$ [33]. $CH_3NH_3PbCl_3$ is not suitable for the absorber layer of efficient PSCs due to its significantly higher energy bandgap than that required to achieve the Shockley-Queisser limit [34]. At the temperature of 100°C, 110°C,

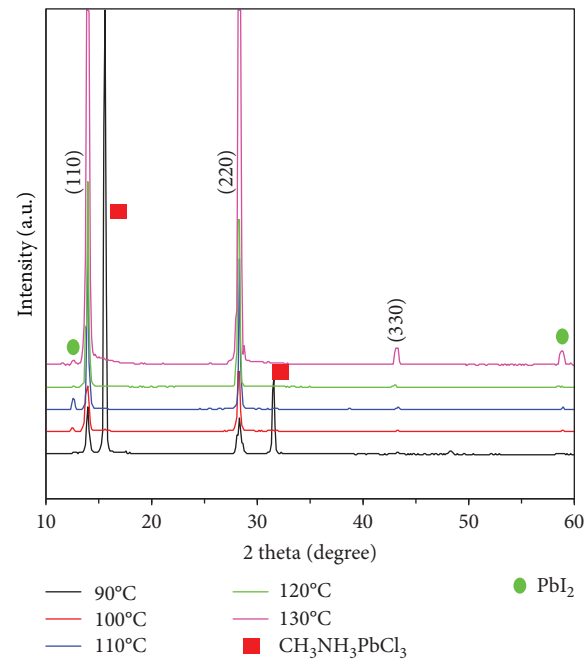

FIGURE 5: XRD patterns of $CH_3NH_3PbI_{3-X}Cl_X$ films annealing at different OS direct annealing temperatures on TiO_2 layers. The red squares and green circles indicate the peaks associated with the $CH_3NH_3PbCl_3$ and PbI_2, respectively.

and 130°C, the diffraction peak that appears at 12.53° can be indexed to the (001) planes of PbI_2. Notably, looking closely at the region of the (110) diffraction peak at 13.99°, there is a small signal of a diffraction peak at 12.53° (the (001) peak for PbI_2) and no measurable diffraction peak at 15.5° (the (100) peak for $CH_3NH_3PbCl_3$), manifesting a high level of phase purity of $CH_3NH_3PbI_{3-X}Cl_X$ films by the annealing temperature of 120°C. Taking into account the SEM images and XRD patterns, we employed 100°C in our investigations.

3.3. Effect of Different Annealing Programs on the Morphology of the Perovskite Film. To further address the effect of the annealing program on the morphology of the perovskite film, two different annealing programs for the ultimate temperature of 100°C, OS, and MS, were adopted for $CH_3NH_3PbI_{3-X}Cl_X$ perovskite film treatment. Samples $CH_3NH_3PbI_{3-X}Cl_X$ (MS) and $CH_3NH_3PbI_{3-X}Cl_X$ (OS) are corresponding to the films manufactured with MS slow and OS direct annealing method, respectively. The XRD patterns and the UV-vis absorption spectra of $CH_3NH_3PbI_{3-X}Cl_X$

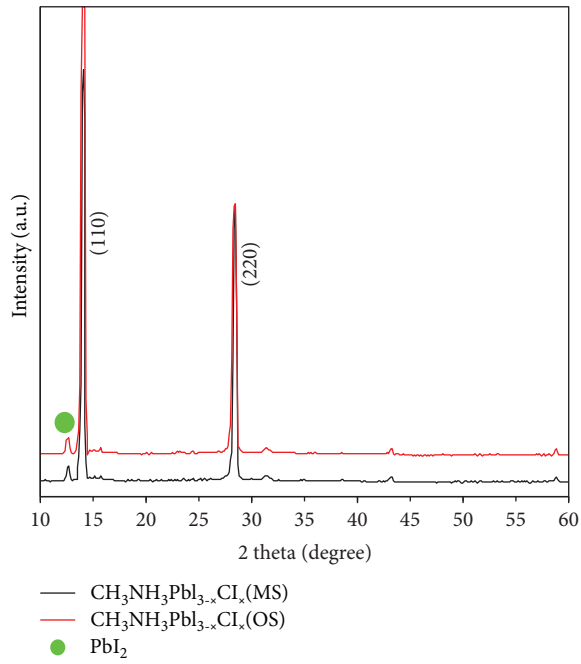

FIGURE 6: XRD patterns of $CH_3NH_3PbI_{3-X}Cl_X$ films deposited on c-TiO_2 layers with two different annealing programs for the ultimate temperature of 100°C. The green circles indicate the peaks of PbI_2.

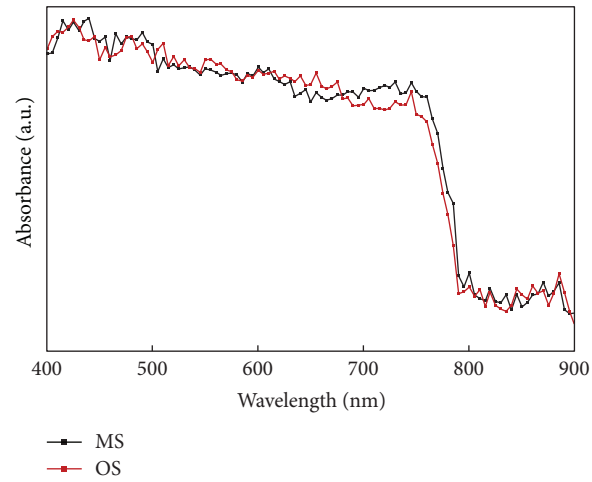

FIGURE 7: UV-vis absorption spectra of $CH_3NH_3PbI_{3-X}Cl_X$ films deposited on TiO_2 layers with two different annealing programs for the ultimate temperature of 100°C.

films deposited on c-TiO_2 layers with two different annealing programs are shown in Figures 6 and 7, respectively. The peaks at 13.99° and 28.36° are assigned to the $CH_3NH_3PbI_{3-X}Cl_X$ phase, revealing that both two anneal methods have fabricated the same orthorhombic perovskite structured $CH_3NH_3PbI_{3-X}Cl_X$ crystals, and the narrow diffraction peaks represent that the films have long-range crystalline domains [3]. No new diffraction peaks or peak shifts are observed, indicating that the crystal structure of the two sintered $CH_3NH_3PbI_{3-X}Cl_X$ films is the same, which is consistent with the previous report [21]. The weak peak centered at 12.53° is attributed to PbI_2, and the $CH_3NH_3PbCl_3$ phase (with a peak at 15.5°) does not appear.

The absorption spectra (Figure 7) manifest the similar light-harvesting capabilities over the visible to near-IR spectrum regardless of the different annealing programs adopted. Both two films exhibit the roughly same absorption edge at about 780 nm (corresponding to ~1.55 eV optical bandgap of $CH_3NH_3PbI_{3-X}Cl_X$), which is consistent with the previous studies [35]. However, the absorption edge of MS film shows a slightly red shift, which should be due to the improved crystallinity with this method [36]. And this result is consistent with the conclusion from Figure 8.

However, the SEM pictures presented for two magnifications (Figure 8) reveal stark differences in perovskite film morphology prepared by two different annealing programs. Compared to the OS film, the film MS shows more homogeneous and dense surface morphology, which has a smaller number of pinholes and grain boundaries. According to the different surface morphologies of the perovskite films treated by the two programs, we can expect different photovoltaic performance of devices. The complete cells, which are named MS-1 and MS-2, are fabricated by MS slow annealing method, and the OS-1 and OS-2 cells are corresponding to the control devices. In the OS devices, Jsc, Voc, and fill factor are lower than the MS cells, as shown in the J-V curves presented in Figure 9. Since the main difference among these cells lies in $CH_3NH_3PbI_{3-X}Cl_X$, the variation of device parameters should be attributed to perovskite films. The significant decrease in these parameters (Table 2) may be a consequence of inferior perovskite film coverage [37]. The bare c-TiO_2 regions (corresponding to the blue circle areas of Figure 8(c)) with no perovskite coverage result in a drop of photocurrent attributing to no light absorption. Furthermore, the larger level of grain boundaries leads to the increase of nonradiative charge carrier recombination, which caused a drop in Voc and FF. The higher parameters of devices by MS method account for a high average PCE (11.43%) values in this paper. The MS slow annealing method is obviously suitable for the preparation of highly efficient PSCs [21], due to the highly homogeneous perovskite structure which enables more uniform charge generation and collection as well as decreases the leakage with fewer shunt paths [37].

3.4. Device Performance with All Optimal Processes. We fabricate two cells by MS slow annealing method for the ultimate temperature of 100°C with optimal c-TiO_2 layer. Detailed photovoltaics data for these two devices extracted from J-V curves (Figure 10) can be found in Table 3. We derive values of 22.33 $mA{\cdot}cm^{-2}$, 0.985 V, and 0.652 for Jsc, Voc, and the fill factor, respectively, yielding a PCE of 14.64% for the best-performance cell measured at a light intensity of $P_{in} = 100\ mW{\cdot}cm^{-2}$.

4. Conclusions

Our work represents a development of c-TiO_2 film depending on spin coating speed and an improvement of $CH_3NH_3PbI_{3-X}Cl_X$ perovskite film relying on the annealing

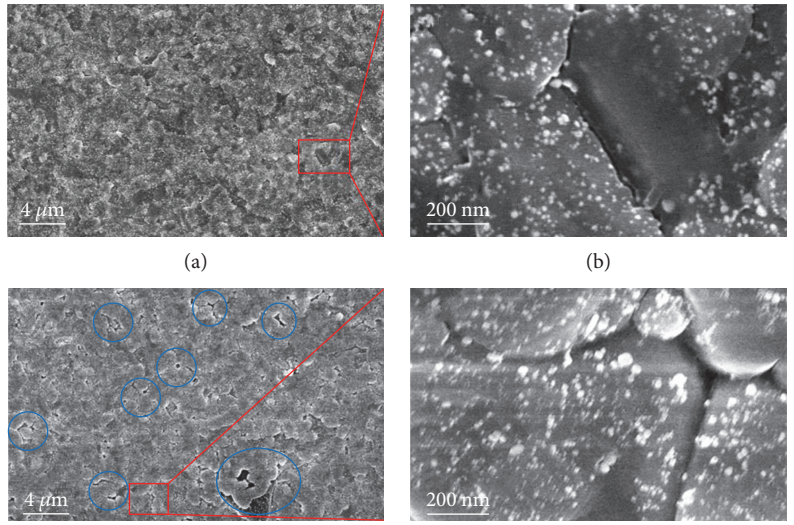

Figure 8: Top view SEM images of $CH_3NH_3PbI_{3-X}Cl_X$ films deposited on the c-TiO_2 layer with two different annealing programs, (a) MS slow and (c) OS direct annealing method. (b) and (d) are the enlarged images of the selected rectangular areas of (a) and (c), respectively.

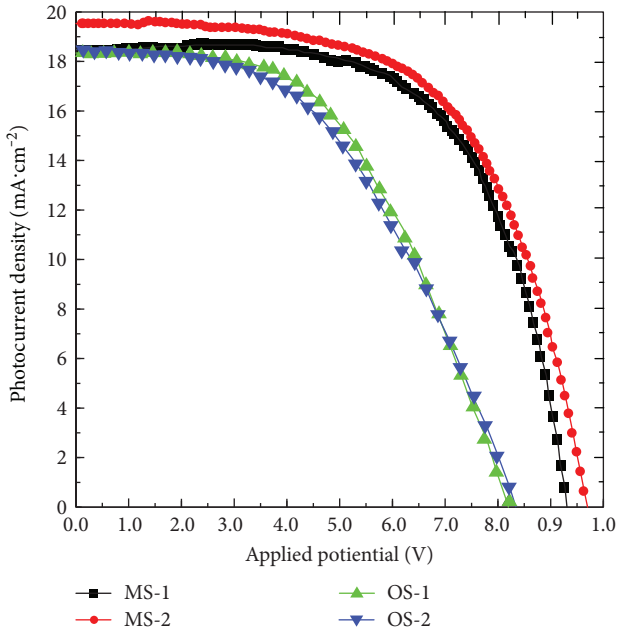

Figure 9: J-V characteristics of devices with $CH_3NH_3PbI_{3-X}Cl_X$ films treated by two different annealing programs.

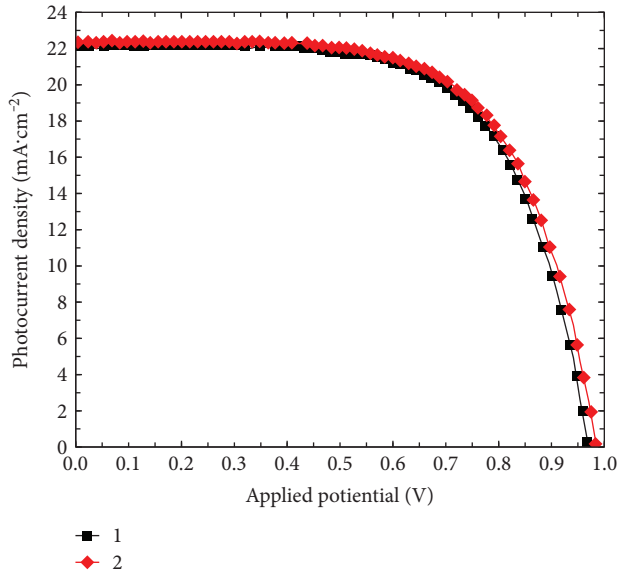

Figure 10: J-V curves of two devices with all optimal processes measured under standard AM 1.5G illumination (100 mW/cm^2).

Table 2: Photovoltaic performance parameters extracted from J-V curves (Figure 9).

Sample	J_{sc}/mAcm^{-2}	V_{oc}/V	FF/%	PCE/%
MS-1	18.44	0.92	0.63	11.15
MS-2	19.53	0.97	0.60	11.7
OS-1	18.34	0.82	0.52	7.94
OS-2	18.46	0.83	0.48	7.57

Table 3: Photovoltaic performance parameters extracted from J-V curves (Figure 10).

Sample	J_{sc}/mA·cm^{-2}	V_{oc}/V	FF/%	PCE/%
1	22.10	0.97	0.576	14.30
2	22.33	0.985	0.652	14.64

process. Emphatically, the morphology and photovoltaic properties of perovskite films produced by two annealing programs are compared. Spin coating of 2000 rpm for 60 s

is found to be the excellent approach for controlling morphology c-TiO_2 film. For the perovskite film, MS slow annealing method is better than OS direct annealing method for the ultimate temperature of 100°C because of the difference in morphology. Compared to the device with OS method, the efficiency is increased from 7.94% to 11.7% for the MS method and to 14.64% for the all optimal processes. This combination of optimal c-TiO_2 and MS slow annealing method for low temperature is expected to help push the organic-inorganic hybrid solar cells closer to commercial feasibility.

Conflicts of Interest

The authors declare that there is no conflict of interests regarding the publication of this paper.

Acknowledgments

This work was partially supported by Project of Natural Science Foundation of China (91233201 and 61376057), Project of Natural Science Foundation of Beijing (Z160002 and 3131001), the Opened Fund of the State Key Laboratory on Integrated Optoelectronics (no. IOSKL2016KF19), Beijing Key Laboratory for Sensors of BISTU (KF20171077203), and Science & Technology Innovation Projects of Master Graduate & Bachelor Student at BISTU.

References

[1] A. Kojima, K. Teshima, Y. Shirai, and T. Miyasaka, "Organometal halide perovskites as visible-light sensitizers for photovoltaic cells," *Journal of the American Chemical Society*, vol. 131, no. 17, pp. 6050-6051, 2009.

[2] H.-S. Kim, C.-R. Lee, J.-H. Im et al., "Lead iodide perovskite sensitized all-solid-state submicron thin film mesoscopic solar cell with efficiency exceeding 9%," *Scientific Reports*, vol. 2, p. 591, 2012.

[3] M. M. Lee, J. Teuscher, T. Miyasaka, T. N. Murakami, and H. J. Snaith, "Efficient hybrid solar cells based on meso-superstructured organometal halide perovskites," *Science*, vol. 338, no. 6107, pp. 643–647, 2012.

[4] M. Liu, M. B. Johnston, and H. J. Snaith, "Efficient planar heterojunction perovskite solar cells by vapour deposition," *Nature*, vol. 501, no. 7467, pp. 395–398, 2013.

[5] W. Ke, G. Fang, J. Wan et al., "Efficient hole-blocking layer-free planar halide perovskite thin-film solar cells," *Nature Communications*, vol. 6, p. 6700, 2015.

[6] N. P. Ariyanto, H. Abdullah, J. Syarif, B. Yuliarto, and S. Shaari, "Fabrication of zinc oxide-based dye-sensitized solar cell by chemical bath deposition," *Functional Materials Letters*, vol. 3, no. 4, pp. 303–307, 2011.

[7] D. Liu and T. L. Kelly, "Perovskite solar cells with a planar heterojunction structure prepared using room-temperature solution processing techniques," *Nature Photonics*, vol. 8, no. 2, pp. 133–138, 2014.

[8] J. Burschka, N. Pellet, S. J. Moon et al., "Sequential deposition as a route to high-performance perovskite-sensitized solar cells," *Nature*, vol. 499, no. 7458, pp. 316–319, 2013.

[9] Z. Li, Y. Zhou, C. Bao et al., "Vertically building Zn_2SnO_4 nanowire arrays on stainless steel mesh toward fabrication of large-area, flexible dye-sensitized solar cells," *Nanoscale*, vol. 4, no. 11, pp. 3490–3494, 2012.

[10] J. Song, E. Zheng, J. Bian et al., "Low-temperature SnO_2-based electron selective contact for efficient and stable perovskite solar cells," *Journal of Materials Chemistry A*, vol. 3, no. 20, pp. 10837–10844, 2015.

[11] J. Y. Jeng, Y. F. Chiang, M. H. Lee et al., "$CH_3NH_3PbI_3$ perovskite/fullerene planar-heterojunction hybrid solar cells," *Advanced Materials*, vol. 25, no. 27, pp. 3727–3732, 2013.

[12] D. Bi, S. J. Moon, L. Häggman et al., "Using a two-step deposition technique to prepare perovskite ($CH_3NH_3PbI_3$) for thin film solar cells based on ZrO_2 and TiO_2 mesostructures," *RSC Advances*, vol. 3, no. 41, pp. 18762–18766, 2013.

[13] Y. Wu, A. Islam, X. Yang et al., "Retarding the crystallization of PbI_2 for highly reproducible planar-structured perovskite solar cells via sequential deposition," *Energy & Environmental Science*, vol. 7, no. 9, pp. 2934–2938, 2014.

[14] Q. Chen, H. Zhou, Z. Hong et al., "Planar heterojunction perovskite solar cells via vapor-assisted solution process," *Journal of the American Chemical Society*, vol. 136, no. 2, pp. 622–625, 2013.

[15] N. J. Jeon, J. H. Noh, W. S. Yang et al., "Compositional engineering of perovskite materials for high-performance solar cells," *Nature*, vol. 517, no. 7535, pp. 476–480, 2015.

[16] H. Zhou, Q. Chen, G. Li et al., "Interface engineering of highly efficient perovskite solar cells," *Science*, vol. 345, no. 6196, pp. 542–546, 2014.

[17] G. Xing, N. Mathews, S. Sun et al., "Long-range balanced electron- and hole-transport lengths in organic-inorganic $CH_3NH_3PbI_3$," *Science*, vol. 342, no. 6156, pp. 344–347, 2013.

[18] C. S. Karthikeyan and M. Thelakkat, "Key aspects of individual layers in solid-state dye-sensitized solar cells and novel concepts to improve their performance," *Inorganica Chimica Acta*, vol. 361, no. 3, pp. 635–655, 2008.

[19] P. Lellig, M. A. Niedermeier, M. Rawolle et al., "Comparative study of conventional and hybrid blocking layers for solid-state dye-sensitized solar cells," *Physical Chemistry Chemical Physics*, vol. 14, no. 5, pp. 1607–1613, 2012.

[20] NREL chart, Rev.04-14-2017, https://www.nrel.gov/pv/assets/images/efficiency-chart.png.

[21] L. Huang, Z. Hu, J. Xu, K. Zhang, J. Zhang, and Y. Zhu, "Multi-step slow annealing perovskite films for high performance planar perovskite solar cells," *Solar Energy Materials and Solar Cells*, vol. 141, pp. 377–382, 2015.

[22] N. N. Zhang, Y. J. Guo, X. Yin, M. He, and X. P. Zou, "Spongy carbon film deposited on a separated substrate as counter electrode for perovskite-based solar cell," *Materials Letters*, vol. 182, pp. 248–252, 2016.

[23] Z. Liu, Q. Chen, Z. Hong et al., "Low-temperature TiO_x-compact layer for planar heterojunction perovskite solar cells," *ACS Applied Materials & Interfaces*, vol. 8, no. 17, pp. 11076–11083, 2016.

[24] J. Park and M. Lee, "Performance enhancement of dye-sensitized solar cell with a $TiCl_4$-treated TiO_2 compact layer," *Electronic Materials Letters*, vol. 11, no. 2, pp. 271–275, 2015.

[25] L. Cojocaru, S. Uchida, Y. Sanehira, J. Nakazaki, T. Kubo, and H. Segawa, "Surface treatment of the compact TiO_2 layer for efficient planar heterojunction perovskite solar cells," *Chemistry Letters*, vol. 44, no. 5, pp. 674–676, 2015.

[26] A. T. Barrows, A. J. Pearson, C. K. Kwak, A. D. F. Dunbar, A. R. Buckley, and D. G. Lidzey, "Efficient planar heterojunction

mixed-halide perovskite solar cells deposited via spray-deposition," *Energy & Environmental Science*, vol. 7, no. 9, pp. 2944–2950, 2014.

[27] W. J. Zeng, X. M. Liu, H. P. Wang, D. Cui, R. Xia, and Y. Min, "Mechanism study on enhanced open-circuit voltage of perovskite solar cells with vapor-induced TiO_2, as electron-transport layer," *Thin Solid Films*, vol. 629, pp. 11–16, 2017.

[28] A. K. Jena, H. W. Chen, A. Kogo, Y. Sanehira, M. Ikegami, and T. Miyasaka, "The Interface between FTO and the TiO_2 compact layer can be one of the origins to hysteresis in planar heterojunction perovskite solar cells," *ACS Applied Materials & Interfaces*, vol. 7, no. 18, pp. 9817–9823, 2015.

[29] W. Ke, G. Fang, J. Wang et al., "Perovskite solar cell with an efficient TiO_2 compact film," *Applied Materials & Interfaces*, vol. 6, no. 18, pp. 15959–15965, 2014.

[30] A. Dualeh, N. Tétreault, T. Moehl, P. Gao, M. K. Nazeeruddin, and M. Grätzel, "Effect of annealing temperature on film morphology of organic-inorganic hybrid pervoskite solid-state solar cells," *Advanced Functional Materials*, vol. 24, no. 21, pp. 3250–3258, 2014.

[31] G. E. Eperon, V. M. Burlakov, P. Docampo, A. Goriely, and H. J. Snaith, "Morphological control for high performance, solution-processed planar heterojunction perovskite solar cells," *Advanced Functional Materials*, vol. 24, no. 1, pp. 151–157, 2014.

[32] Z. L. Zhang, B. Q. Men, Y. F. Liu, H. P. Gao, and Y. L. Mao, "Effects of precursor solution composition on the performance and I-V hysteresis of perovskite solar cells based on CH3NH3PbI3-xClx," *Nanoscale Research Letters*, vol. 12, no. 84, p. 8, 2017.

[33] N. Kitazawa, Y. Watanabe, and Y. Nakamura, "Optical properties of $CH_3NH_3PbX_3$ (X = halogen) and their mixed-halide crystals," *Journal of Materials Science*, vol. 37, no. 17, pp. 3585–3587, 2002.

[34] Y.-C. Chern, Y.-C. Chen, H.-R. Wu, H. W. Zan, H. F. Meng, and S. F. Horng, "Grain structure control and greatly enhanced carrier transport by $CH_3NH_3PbCl_3$, interlayer in two-step solution processed planar perovskite solar cells," *Organic Electronics*, vol. 38, pp. 362–369, 2016.

[35] D. Wang, Z. Liu, Z. Zhou et al., "Reproducible one-step fabrication of compact $MAPbI_{3-x}Cl_x$ thin films derived from mixed-lead-halide precursors," *Chemistry of Materials*, vol. 26, no. 24, pp. 7145–7150, 2014.

[36] D. Liu, L. Wu, C. Li et al., "Controlling $CH_3NH_3PbI_{(3-x)}cl_{(x)}$ film morphology with two-step annealing method for efficient hybrid perovskite solar cells," *ACS Applied Materials & Interfaces*, vol. 7, no. 30, pp. 16330–16337, 2015.

[37] Y. Yang, S. Feng, M. Li et al., "Annealing induced recrystallization in $CH_3NH_3PbI_{3-x}Cl_x$ for high performance perovskite solar cells," *Scientific Reports*, vol. 7, no. 46724, p. 9, 2017.